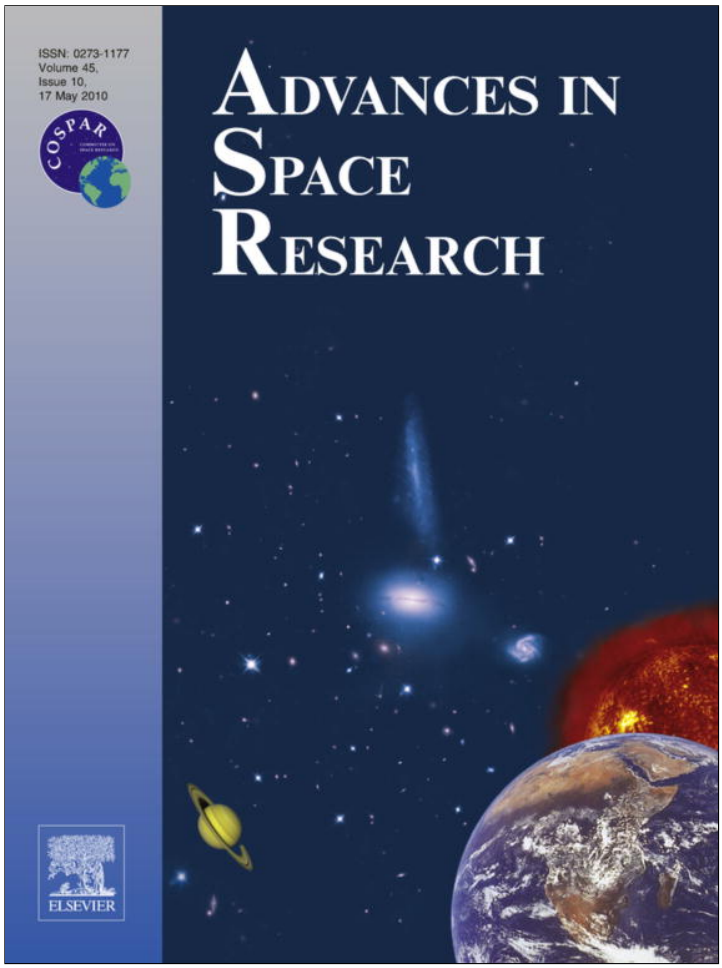

Available online at www.sciencedirect.com
ScienceDirect
Advances in Space Research 45 (2010) 1268–1275
ADVANCES IN SPACE RESEARCH (a COSPAR publication)
www.elsevier.com/locate/asr

The distributions of the OH Meinel and $O_2(a^1\Delta–X^3\Sigma)$ nightglow emissions in the Venus mesosphere based on VIRTIS observations

J.-C. Gérard [a,*], L. Soret [a], A. Saglam [a], G. Piccioni [b], P. Drossart [c]

[a] Laboratoire de Physique Atmosphérique et Planétaire, Université de Liège, 17, allée du 6 aout, B-4000 Liège, Belgium
[b] IASF-INAF, Via del Fosso del Cavaliere 100, I-00133 Roma, Italy
[c] Observatoire de Paris, Place Jules Janssen 5, F-92190 Meudon, France

Received 19 May 2009; received in revised form 20 November 2009; accepted 18 January 2010

Abstract

$O_2(a^1\Delta)$ and recently discovered OH Meinel nightglow emissions have been observed at the limb with the Visible and Infrared Thermal Imaging Spectrometer (VIRTIS-M) instrument on board the Venus Express satellite. Hydroxyl bands belonging to $\Delta v = 1$ sequence between 2.60 and 3.14 μm and to $\Delta v = 2$ sequence at 1.40–1.46 μm have been unambiguously identified. In this study, we analyze the statistical distribution of the $\Delta v = 1$ OH Meinel band sequence and the $a^1\Delta_g - X^3\Sigma$ (0–0) band of the O_2 Infrared Atmospheric bands at 1.27 μm. We also present an analysis of the correlation between the two emissions. From a statistical point of view, we find that the limb intensity of both emissions reach their maximum value near the antisolar point, while they are significantly dimmer in the vicinity of the terminator. The average altitude of the limb emissions peaks are 95.3 ± 3 km and 96 ± 2.7 km, respectively for the OH $\Delta v = 1$ sequence and $O_2(a^1\Delta)$ emissions. The average intensities are 0.41 ± 0.37 MR and 28 ± 22 MR, respectively, corresponding to a mean ratio of about 70. The altitude of the OH nightglow layer is closely related to that of the $O_2(a^1\Delta)$ emission and some level of co-variation of the maximum intensity along the line of sight is observed. It is suggested that the global subsolar to antisolar circulation plays a key in the control of both airglows by carrying oxygen atoms from the day to the night side of the planet. The O atoms recombine to produce $O_2(a^1\Delta)$ molecules and they also act as precursors of ozone whose reaction with H produces excited hydroxyl.

Keywords: Venus; Airglow; OH; O_2; Infrared emission; Atmosphere dynamics

1. Introduction

The presence of the OH (2–0), (1–0), (2–1) and possibly (3–2) Meinel bands has been recently identified by Piccioni et al. (2008) in the Venus atmosphere using infrared limb observations made with the Visible and Infrared Thermal Imaging Spectrometer (VIRTIS) on board Venus Express. It was found that the limb intensities are 880 ± 90 kiloRayleighs (kR) for the (1–0) band and 100 ± 40 kR for the OH (2–0) band. The emission layer peaks at an altitude of 96 ± 2 km near midnight, in the case of the orbit used for the analysis. Taking these characteristics into account and assuming a conversion factor of 55.4 between limb and the vertical observations, the associated vertical emission rates were estimated to be 16 kR and 1.8 kR, respectively. These emission rates are 55 ± 5 and 480 ± 200 times weaker than the $O_2(a^1\Delta)$ (0–0) band intensity at 1.27 μm (Piccioni et al., 2008). For a total of 10 orbits examined, these ratios vary from orbit to orbit by ±50%, but the peak altitude appeared to remain constant within the vertical resolution of the measurements. The OH (1–0) P1(4.5) and (2–1) Q1(1.5) OH airglow lines were recently detected by Krasnopolsky (2010) using a ground-based

* Corresponding author. Tel.: +32 4 366 9775; fax: +32 4 366 9711.
E-mail address: jc.gerard@ulg.ac.be (J.-C. Gérard).

0273-1177/$36.00 © 2010 COSPAR. Published by Elsevier Ltd. All rights reserved.
doi:10.1016/j.asr.2010.01.022

telescope. The total hydroxyl emission rate f derived from these observations is consistent with the value obtained by Piccioni et al. (2009).

The O_2 $a^1\Delta$–$X^3\Sigma$ (0–0) band emission at 1.27 μm has been described in considerably more detail. It was first observed on Venus more than 30 years ago (Connes et al., 1979) using Fourier transform spectroscopy from the ground. Spatially resolved ground-based observations (Allen et al., 1992; Crisp et al., 1996; Lellouch et al., 1997; Ohtsuki et al., 2008; Bailey et al., 2008a,b) have demonstrated that the spatial distribution of the $O_2(a^1\Delta)$ infrared airglow is quite variable in space and time. The O_2 (a–X) airglow shows regions of enhanced emission which are usually 1000–2000 km wide. Nightside images indicate that these rapidly changing bright areas occur most frequently at low latitudes between midnight and 03:00 local time. During the Venus flyby by Galileo, Drossart et al. (1993) observed with the Near-Infrared Mapping Spectrometer (NIMS) a large enhancement of the 1.27 μm emission near 40°S, over a spatial area ~100 km wide. The apparent motion of gas masses transported by horizontal winds has been analyzed by Hueso et al. (2008) using the O_2 (a–X) airglow. This study showed that the details of the distribution changed over 30 min, but indicated that large structures usually survive for several hours. Gérard et al. (2008) presented a statistical map of the average $O_2(a^1\Delta)$ infrared nightglow in the southern hemisphere observed with VIRTIS over an 11-month period of low solar activity. They found that the distribution is characterized by an enhanced brightness region located near the midnight meridian at low latitude. The location of the bright airglow region was further studied by Piccioni et al. (2009) who confirmed that it is centered on the anti-solar point. They also analyzed the statistical distribution of the $O_2(a^1\Delta)$ infrared airglow using both nadir and limb viewing geometries. Drossart et al. (2007a) determined that the $O_2(a^1\Delta)$ peak emission is located near 96 km, which is consistent with excitation by three-body recombination of oxygen atoms proposed by Connes et al. (1979):

$$O + O + CO_2 \rightarrow O_2^* + CO_2 \quad (1)$$

which gives rise to radiative deexcitation of the $O_2(a^1\Delta)$ molecules and collisional quenching:

$$O_2^* + CO_2 \rightarrow O_2 + CO_2 \quad (2)$$

Gérard et al. (2008) found that limb profiles observed at northern mid-latitudes exhibit large intensity variations over short time periods. They compared the limb profiles to those obtained with a one-dimensional chemical-diffusive model. The altitude of the peak and its intensity were well reproduced by the model, but the width of the airglow layer was narrower than in the numerical simulation. Piccioni et al. (2009) illustrated the variability and the complexity of the observed airglow limb profiles. They showed that the altitude, the brightness and the width of the emission peak sometimes vary systematically with latitude. They also argued that a secondary peak, possibly generated by upward propagating gravity waves, may be present above 100 km. The O_2(a–X) airglow emission has been used to infer the oxygen density distribution at different locations using the Abel inversion (Gérard et al., 2009).

Two chemical reactions have been proposed so far (Piccioni et al., 2008) as possible sources of excited hydroxyl molecules. The first one is the Bates-Nicolet mechanism (Bates and Nicolet, 1950) occurring in the terrestrial atmosphere:

$$H + O_3 \rightarrow OH^* + O_2 \quad (3)$$

where OH* denotes a hydroxyl molecule in a vibrationally excited level of the $X\ ^2\Pi$ state.

The second one involves hydrogen peroxide and atomic oxygen:

$$HO_2 + O \rightarrow OH^* + O_2 \quad (4)$$

On Earth, the first process leads to the formation of vibrationally excited OH near the mesopause. It preferentially populates the $v = 6$–9 vibrational levels. In the Mars and Venus atmospheres, subsequent radiation and collisional quenching by CO_2 are thought to populate the lower v levels. Reaction (4) does not play a major role in the terrestrial mesosphere (Dodd et al., 1994; Meriwether, 1989), but could be a source of vibrationally excited OH in the Venus mesosphere, where the ozone abundance is smaller. Piccioni et al. (2008) suggested that these reactions contribute to the observed OH emissions on the Venus nightside. They argued that the observed intensity variability may be related to the dependence on temperature of both the efficiency of the production reactions and collisional quenching. In addition, variability in the HO_2, H, O, and O_3 densities can also be important. Similar sensitivity of OH and O_3 to temperature variations has been reported in model calculations for Mars (Zhu and Yee, 2007). Profiles of OH airglow emission calculated from a model (Pernice et al., 2004) show reasonable agreement with the observations both in brightness and vertical distribution, with some deviations.

In this study, we determine the statistical properties of the $\Delta v = 1$ Meinel OH nightside emission and their relationships to the $O_2(a^1\Delta)$ Venus night airglow at 1.27 μm observed during the same time period. This analysis is based on limb profiles obtained with the VIRTIS spectral imager on board Venus Express. We compare the vertical and latitudinal distributions of the OH airglow with those obtained for the $O_2(a^1\Delta)$ emission.

2. Observations

VIRTIS is an imaging spectrometer on board the Venus Express satellite orbiting Venus on a highly elliptical polar orbit with a period of 24 h, an initial pericenter of 250 km from the planet surface at 80°N, and an apocenter at 66,000 km. The orbital configuration and different science missions have been described elsewhere (Svedhem et al., 2007; Titov et al., 2006; Drossart et al., 2007b). The

VIRTIS instrument consists of two spectrometers (Piccioni et al., 2009): VIRTIS-M devoted to spectral mapping, and VIRTIS-H a high-resolution spectrometer. VIRTIS-M utilizes two different detectors, a silicon charge coupled device for the visible channel covering the 0.25–1 μm wavelength range and a HgCdTe infrared focal plane array for the infrared channel covering the 1–5 μm wavelength range. Using a scanning mirror, VIRTIS-M progressively builds up two-dimensional images for each of the 432 spectral bands with a width of 9.5 nm to cover the 1–5 μm wavelength range. It thus provides a data cube of dimensions $432 \times N_s \times N_l$, where N_s and N_l are the dimensions of the image for each spectral band. N_l is related to the length of the observation. N_s has a fixed value, usually equal to 256. For 8-s exposures, the acquisition time of a full 256×256 pixels image takes about 50 min. However, to increase the SNR, binning values of 2 or 4 are occasionally used, giving then a N_s of 128 and 64, respectively and decreasing the total acquisition time accordingly. The field of view of one VIRTIS-M detector pixel is 0.25 mrad, thus covering a total field of 64×64 mrad^2 for a 256×256 pixel image. For a typical slant distance of 7000 km in a limb observation geometry, a pixel corresponds to a spatial extent of 1.75 km. In a nadir observation, this value reaches 15 km at a distance of 60,000 km from the planet. The absolute pointing accuracy is better than ±1/7th of a pixel (Piccioni et al., 2009).

We have used 28 VIRTIS limb image cubes from 21 orbits for the study of OH limb emissions, collected between 17 January 2007 (orbit 271) and 4 January 2008 (orbit 623), thus covering a period of nearly one year. A larger set of limb observations has been used for the O_2 airglow, covering a period of 21 months extending from 6 July 2006 (orbit 76) to 5 April 2008 (orbit 715) and corresponding to 91 VIRTIS-M image cubes from 54 orbits. The signal at the limb corresponding to the OH emission may be less than or comparable to the instrumental background, unlike the O_2 emission at 1.27 μm which is significantly brighter. Consequently, only one third of the total limb OH observations could be used in this study to characterize the OH emissions. The different number of limb profile observations for the two emissions therefore stems from the shorter time period of the OH database and from the weaker intensity of the hydroxyl emission in the range 2.60–3.14 μm.

3. OH and $O_2(a^1\Delta)$ airglow limb profiles

3.1. Profile extraction

All VIRTIS-M observations are data cubes, where the third dimension is wavelength, so that for each selected wavelength a two-dimensional image is obtained. Limb profiles may be extracted from these two-dimensional images using some criteria usually based on the latitude or the local time parameter. However, in some cases the latitude does not vary dramatically while the local time covers a broad range, and in some other cases the opposite occurs. In this study, we use another parameter to extract limb profiles: the angular abscissa α associated to each pixel. This angular abscissa α represents the angle between the direction pointing from the planetary center toward the tangent point of the line of sight and the direction of the pixel of the lower-left corner of the image. Each image is then divided into bands of increasing angular abscissa of width $d\alpha$. Each such α band provides a series of pixels which are subsequently sorted according to the value of their tangent altitude. These points are then grouped into 1 km altitude bins to generate the limb profile associated with this particular band of α value. Each limb profile so defined offers the advantage to span a limited range of latitudes and local times of the tangent points. Using a $d\alpha$ of 1°, up to 45 profiles may be extracted from a 256×256 limb image. Finally, 334 limb profiles for the hydroxyl and 1843 for the $O_2(a^1\Delta)$ emissions respectively have been extracted. Data used for this study are based on the VIRTIS geometry and calibrated data archive files. The subtraction of the instrumental background signal is thus made through the VIRTIS data processing pipeline described in Drossart et al. (2007b). A small residual background contribution is however still occasionally present in the extracted limb profiles above the altitude of the airglow emissions. It is removed by calculating the average value of the residual signal above 120 km for each individual profile and subtracting it from the corresponding limb profile. Finally, the peak signal associated with the airglow emissions is determined for each profile. Only those profiles where the signal at the peak exceeds three times the average high-altitude residual signal are retained. Finally, each limb profile is visually inspected to remove those presenting spurious instrumental noise that makes them inappropriate to be included into the database. In particular, profiles where an atmospheric thermal component in present in the 2.60–3.14 μm range as a result of scattering by haze or high-altitude clouds have been removed. This thermal contribution was shown to be negligible above ~90 km for the O_2 (a–X) emission at 1.27 μm (Piccioni et al., 2009).

Fig. 1 illustrates an example of a bright spectrum showing the presence of the O_2 $a^1\Delta - X^3\Sigma$ (0-0) and (0-1) bands at 1.27 μm and 1.58 μm, respectively. To optimize the signal to noise ratio, we use the (0–0) band to investigate the characteristics of the O_2 nightside airglow. The presence of the Meinel OH bands belonging to the $\Delta v = 1$ sequence is clearly observed between 2.60 and 3.14 μm.

The limb brightness of the emission I_λ at a given wavelength λ is initially expressed in units of W m^{-2} μm^{-1}sr^{-1}. To calculate the brightness B of the total emission in Rayleighs (1R = 10^6 photons cm^{-2} s^{-1} in 4π steradians) within the wavelength range $\lambda_1 - \lambda_2$, we use the conversion formula:

$$B = 1 \times 10^{-10} \frac{4\pi}{hc} \int_{\lambda_1}^{\lambda_2} I_\lambda \lambda \, d\lambda \tag{5}$$

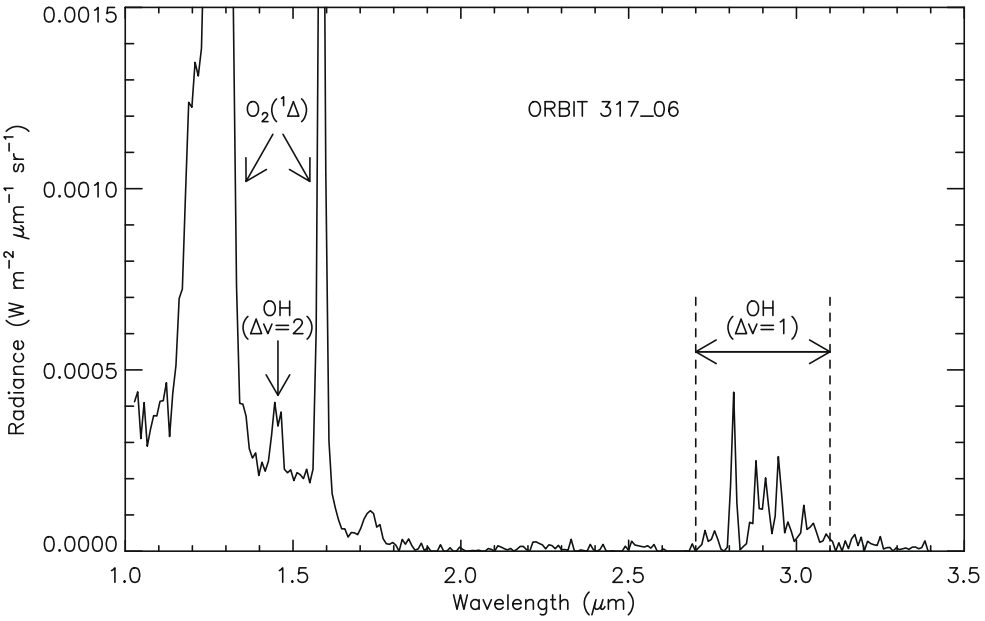

Fig. 1. Example of nightside airglow spectrum obtained during orbit 317-06 acquired on March 4, 2007 between 15° and 25° N. The wavelengths of the O_2 ($a^1\Delta$)–$X(^3\Sigma)$ (0–0) and (0–1) bands at 1.27 μm and 1.58 μm are indicated. The bands between 2.7 and 3.1 μm belong to the $\Delta v = 1$ sequence of the OH Meinel bands. They have been summed up to study the altitude and intensity distributions of this emission along the line of sight of the VIRTIS instrument observing at the limb.

whose discretized form is

$$B = 1 \times 10^{-10} \frac{4\pi}{hc} \Delta\lambda \sum_{\lambda=\lambda_1}^{\lambda=\lambda_2} I_\lambda \lambda \tag{6}$$

$$\simeq 6 \times 10^{13} \sum_{\lambda=\lambda_1}^{\lambda=\lambda_2} I_\lambda \lambda \tag{7}$$

with: $h = 6.62 \times 10^{-34}$ J s, the Planck's constant,

$c = 3 \times 10^8$ m s^{-1}, the speed of light,

$\Delta\lambda = 9.5 \times 10^{-3}$ μm, the width of the VIRTIS-M-IR spectral channel,

I_λ, the intensity in a given pixel of the calibrated data cube in W m^{-2} μm^{-1} sr^{-1},

λ, the wavelength of the emission in μm.

The dimensionless factor 1×10^{-10} appearing in Eqs. (5) and (6) is present for unit compatibility between the two members of the equation when B is expressed in Rayleighs.

For $O_2(a^1\Delta)$, $\lambda_1 = \lambda_2 = 1.27$ μm, for OH, $\lambda_1 = 2.7$ μm, $\lambda_2 = 3.1$ μm.

Unlike observations made in the nadir direction, no correction for scattering by the underlying clouds or scattering by haze is applied to observations made with a tangent altitude larger than 85–90 km (Piccioni et al., 2009).

3.2. Emission characteristics and correlations

Fig. 2 shows the coverage of the 1843 limb profiles extracted for the O_2(a–X) emission. The northern hemisphere is well covered between latitudes of 0° and 80°. All nightside local times from 19:00 to 05:00 are represented as well with, however, more data available on the morning side. The same latitude range is covered by the hydroxyl profiles, while the local time is well covered from 00:00 to 03:00 and poorly before midnight, from 21:30 to 22:00 and 22:30 to 23:30 LT.

Fig. 3 shows the histogram of the tangent altitudes of the maximum limb brightness for both O_2 and OH emissions, grouped into 2 km altitude bins. The distribution is slightly asymmetric around the mean peak altitude of 95.3 ± 3 km and 96 ± 2.7 km for OH and $O_2(a^1\Delta)$, respectively. The distributions of both emissions are very similar, showing that the emission layers are located close to each other within a difference of about 1 km. However, the observed altitude of the O_2 emission peak can reach 105 km, while in the case of the OH emission, the highest observed value is only 102 km.

The distributions of the maximum brightness along the line of sight shown in Fig. 4 are, however, different. They both show a very asymmetric distribution around their average brightness values along the line of sight of 0.41 ± 0.37 MR and 28 ± 23 MR for OH and $O_2(a^1\Delta)$, respectively. The most likely observed value, i.e. the mode of the distribution, is the same as the average in the case of OH, while it is significantly smaller than the average value of the O_2 distribution. The O_2(a–X) peak brightness distribution extends from a few megaRayleighs to as much as 140 MR with a mode at 10 MR. As for OH, the peak brightness distribution extends from tens of kiloRayleighs to 2 MR with a mode at 0.4 MR.

The presence of a bright spot centered on the antisolar point in the average intensity map of the O_2 (a–X) emission (Gérard et al., 2008; Piccioni et al., 2009) suggests to use the angular distance from the antisolar point (hereafter

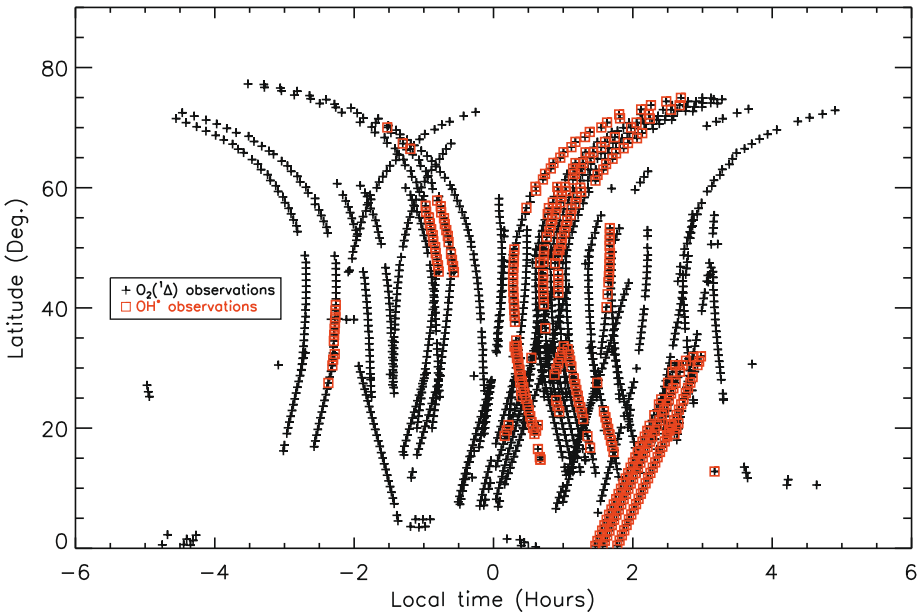

Fig. 2. Latitude-local time distribution of the limb observations of the $O_2(a^1\Delta)$ (in black) and OH Meinel (in red) emissions used in this study.

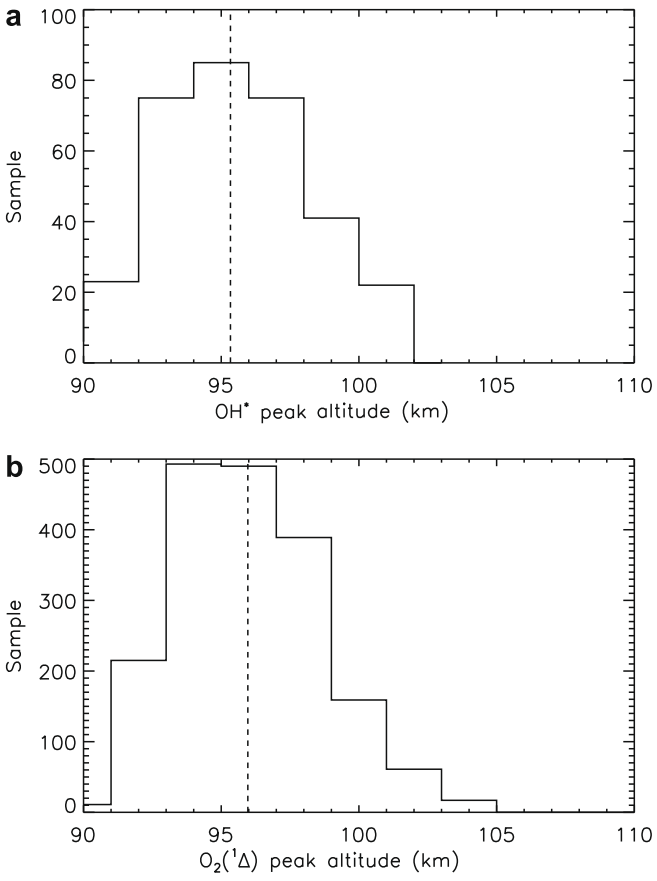

Fig. 3. Distribution of the peak altitudes along the line of sight of the nightside OH Meinel (a) and $O_2(a^1\Delta)$ (b) emissions observed at the limb with VIRTIS-M. The vertical dotted line shows the mean value of the distribution.

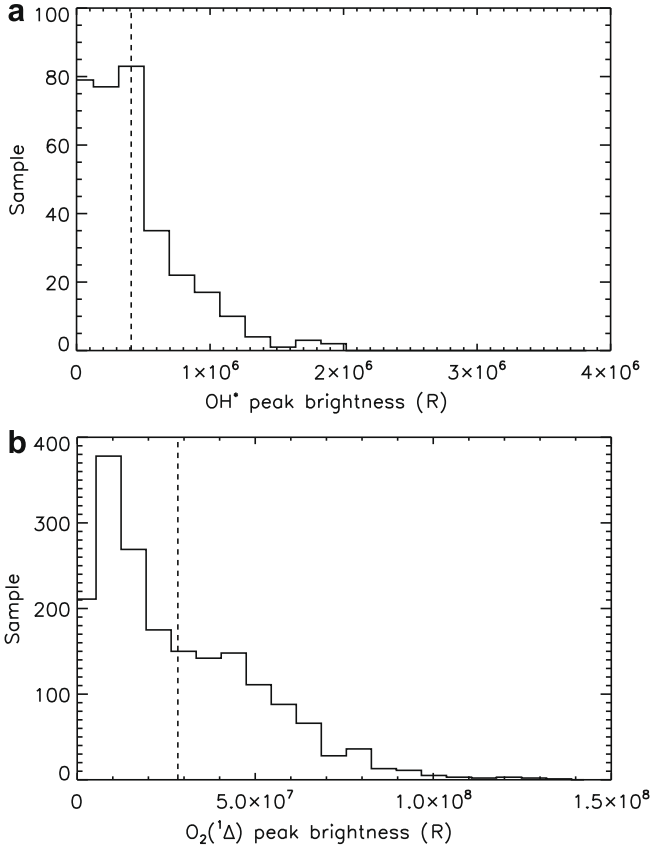

Fig. 4. Distribution of the maximum brightness measured along the line of sight of the nightside OH Meinel (a) and $O_2(a^1\Delta)$ (b) emissions observed at the limb with VIRTIS-M. The vertical dotted line shows the mean value of the distribution.

referred to as the antisolar angle) as the natural variable for the study of the limb peak brightness and altitude variations in the Venus atmosphere. In Fig. 5, the maximum brightness along the line of sight is plotted versus the

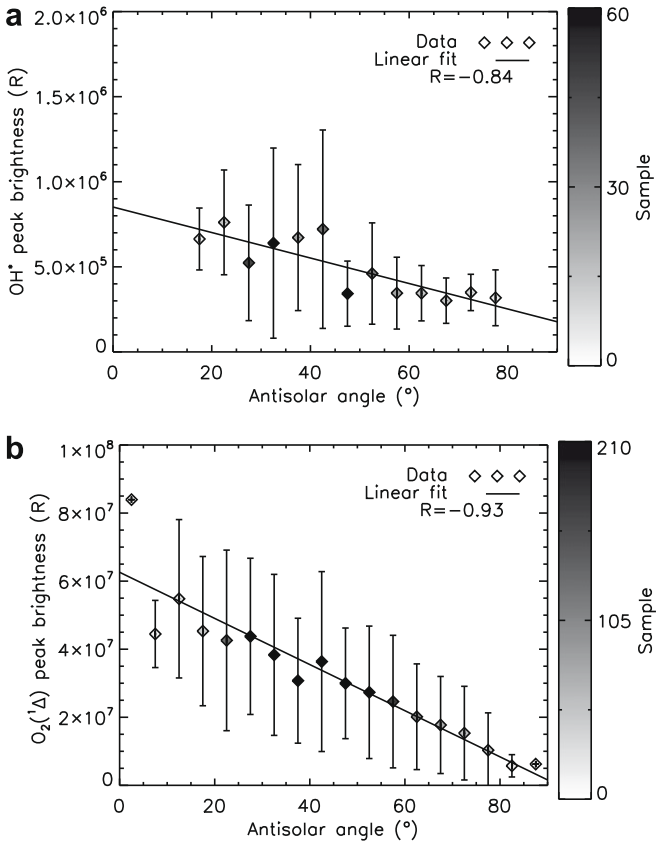

Fig. 5. Statistical distribution of the observed maximum limb brightness of the OH (a) and $O_2(a^1\Delta)$ (b) infrared nightglow as a function of the antisolar angle. The observations have been grouped into 5° angular bins. The central values in each bin are the mean values and the vertical bars indicate the (1-σ variability in the bins. The solid line shows the linear regression through the data points and R is the value of the correlation coefficient for the binned data.

antisolar angle. For the clarity of the figure, the individual values have been grouped into 5° antisolar angle bins and the average values are plotted at the center of each bin. The 1-σ standard deviations in each bin are shown by vertical bars to indicate the importance of the variability around the average values. A large variability appears at each angle value although it does not affect the general trend. The darkness of the grey zone filling the diamond symbols indicates the number of samples in each angular bin. A decrease of the limb peak brightness for $O_2(a^1\Delta)$ as well as for the OH emissions is observed from the antisolar point to the terminator. The linear least-squares regression line plotted through the data points is associated with high correlation coefficients R equal to -0.84 and -0.93 for OH and O_2, respectively. These values refer to the correlation between the central values in each bin. To test the significance of these correlations, we also calculate the correlation coefficient r for the linear regression through the individual data points. The r values are -0.30 for OH and -0.43 for O_2, respectively. To assess the significance of these correlation coefficients, we test the null hypothesis, that is the level of confidence that r is significantly different from zero. Since the number of samples used for each plot in Figs. 5–7 exceeds 100, r is normally distributed around 0 for two non-correlated variables and the 1-σ standard deviation of r is given by $s_0 = 1/\sqrt{(n-1)}$, where n is the number of observations. Comparing the r values to s_0, we find that both correlation coefficients are significantly different from 0 at a confidence level exceeding 99.99 percent. In Fig. 6, a similar plot shows the dependence of the tangent altitudes of maximum emission versus the latitude of the tangent point. The altitude of the maximum emission along the line of sight of the O_2(a–X) emission appears to increase with latitude by about 2–3 km, with a correlation coefficient of 0.67 for the binned data. For the OH nightglow, the altitude of the peak emission along the line of sight also shows a general increase from 94 to 98 km between 0° and 75° with a correlation coefficient $R = 0.81$ for the binned observations. The values of the r linear correlation coefficient for the individual measurements are 0.37 for OH and 0.23 for O_2 airglows. Consequently, the confidence level that the r values are different from zero again exceeds 99.99 percent.

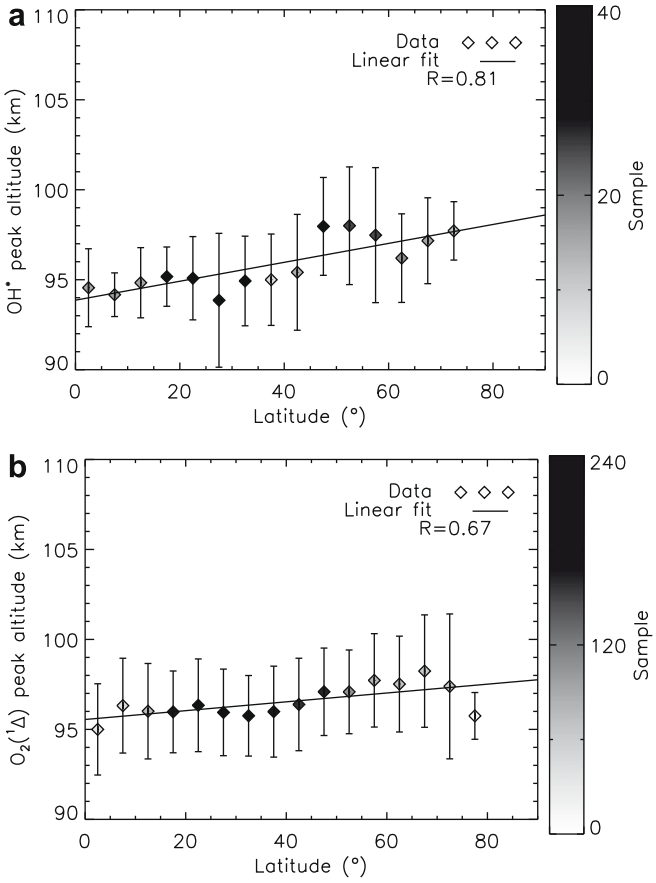

Fig. 6. Statistical variation of the altitude of the maximum limb brightness of the OH (a) and $O_2(a^1\Delta)$ (b) infrared nightglow as a function of latitude. The observations have been grouped into 5° latitudinal bins. The central values in each bin are the mean values and the vertical bars indicate the 1-σ variability in the bins. The solid line shows the linear regression through the data points and R is the value of the correlation coefficient for the binned data.

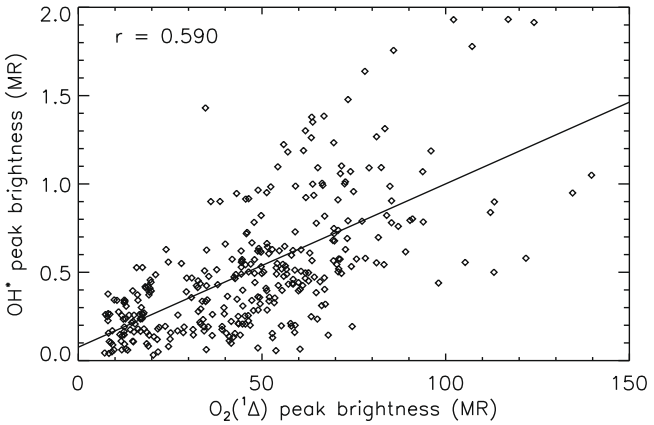

Fig. 7. Relationship between the maximum limb brightness of individual simultaneous OH and $O_2(a^1\Delta)$ limb profiles. The solid line shows the linear regression through the individual observations and r is the value of the correlation coefficient.

Finally, Fig. 7 illustrates the correlation between the peak brightness along the line of sight of the two emissions. Each data point corresponds to a simultaneous limb observation of the two emissions. The plot and the linear correlation coefficient $r = 0.59$ suggest the presence of a correlation between the brightness of the OH and the $O_2(a^1\Delta)$ emissions. Comparison with the value of s_0 indicates that the correlation coefficient is different from zero at the 99.99 percent confidence level.

4. Discussion and conclusion

Our statistical study of the OH Meinel and $O_2(a^1\Delta_g–X^3\Sigma)$ airglow limb observations indicates a great deal of similarities between the two emissions. The altitude distributions are nearly identical, both exhibiting a maximum with a statistical altitude separation as small as ~1 km. Both airglow features present an asymmetric distribution about their mean peak brightness values. Part of this asymmetry in the OH airglow intensity probably stems from the removal from the database of those limb profiles with a low level signal compared to the background level in the 2.7–3.1 μm region. The distribution of the maximum brightness of the $O_2(a^1\Delta)$ limb emission extends from a few megaRayleighs to as much as 140 MR with a mode at 10 MR. As for OH $\Delta v = 1$ sequence emission, its distribution of the maximum peak brightness spans values from tens of kiloRayleigh to 2 MR with a mode at 0.4 MR. The similarity between the altitudes of the peak intensity along the line of sight of the two airglows and the correlation between their brightness variations initially suggested chemical reactions involving $O_2(a^1\Delta)$ to be the primary source of OH. However, those chemical reactions fail by far to reproduce the observed OH intensity. Further modelling work is needed to examine if and why the $O_3 + H$ reaction produces an airglow layer showing similarities to the $O_2(a^1\Delta)$ emission. It is clear that atomic oxygen is a common precursor to reaction (1) and to the formation of ozone. When O atoms are transported from the dayside where they have been created by photodissociation of CO_2, they recombine to produce the O_2 airglow (Bougher et al., 2006). They tend to statistically accumulate near the antisolar point where the O density appears to maximize in the upper mesosphere (Gérard et al., 2009). At the same time, they participate in reactions involving minor constituents to produce O_3 which, in turn, reacts with H to produce excited OH molecules. Transport of atomic oxygen may therefore explain why the OH airglow peak tends to be located close to the O_2(a–X) airglow maximum. Support for this scenario is provided by the recent detection of ozone in the Venus nighttime lower thermosphere (Montmessin et al., 2009) based on stellar occultations with the SPICAV ultraviolet spectrograph. The observations suggest the presence of O_3 densities up to about 1×10^{10} cm^{-3} near 100 km.

Further progress in this question and a detailed assessment of the relative role of reactions (3) and (4) require detailed modelling of the O, O_3 and H distributions, including transport from the dayside and detailed nightside photochemistry. An initial estimate by Krasnopolsky (2010) based on a one-dimensional model involving 21 species and 54 reactions has lead to the conclusion that reaction (3) is more efficient by an order of magnitude than (4) in producing the hydroxyl airglow. It is likely that the coupling between the subsolar to antisolar global circulation, local turbulent transport and photochemistry all play a role in the vertical and horizontal distribution of the species producing the excited hydroxyl molecules.

Acknowledgments

We gratefully thank all members of the ESA Venus Express project and of the VIRTIS scientific and technical teams. J.C.G. acknowledges funding from the Belgian Fund for Scientific Research (FNRS). A. Saglam and L. Soret were supported by the PRODEX program managed the European Space Agency with the help of the Belgian Federal Space Science Policy Office. This work was funded by Agenzia Spaziale Italiana and the Centre National d'Etudes Spatiales.

References

Allen, D., Crisp, D., Meadows, V. Variable oxygen airglow on Venus as a probe of atmospheric dynamics. Nature 359, 516–519, 1992.

Bates, D.J., Nicolet, M. The photochemistry of atmospheric water vapor. J. Geophys. Res. 55, 301–327, 1950.

Bailey, J., Meadows, V.S., Chamberlain, S., Crisp, D. The temperature of the Venus mesosphere from O_2 ($a^1\Delta_g$) airglow observations. Icarus 197, 247–259, doi:10.1016/j.icarus.2008.04.007, 2008a.

Bailey, J., Chamberlain, S., Crisp, D., Meadows, V.S. Near infrared imaging spectroscopy of Venus with the Anglo-Australian Telescope. Planet. Space Sci. 56, 1385–1390, doi:10.1016/j.pss.2008.03.006, 2008b.

Bougher, S.W., Rafkin, S., Drossart, P. Dynamics of the Venus upper atmosphere: outstanding problems and new constraints expected from Venus Express. Planet. Space Sci. 54, 1371–1380, 2006.

Connes, P., Noxon, J.F., Traub, W.A., Carleton, N.P. $O_2(^1\Delta)$ emission in the day and night airglow of Venus. Astrophys. J. 233, L29–L32, 1979.

Crisp, D., Meadows, V.S., Bézard, B., de Bergh, C., Maillard, J.-P., Mills, F.P. Ground-based near-infrared observations of the Venus nightside: 1.27-μm $O_2(a^1\Delta)$ airglow from the upper atmosphere. J. Geophys. Res. 101, 4577–4593, 1996.

Dodd, J.A., Lipson, S.J., Lowell, J.R., Armstrong, P.S., Blumberg, W.A.M., Nadile, R.M., Adler-Golden, S.M., Marinelli, W.J., Holtzclaw, K.W., Green, B.D. Analysis of hydroxyl earthlimb airglow emissions: kinetic model for state-to-state dynamics of OH (v,N). J. Geophys. Res. 99, 3559–3585, 1994.

Drossart, P. et al. Search for spatial variations of the H_2O abundance in the lower atmosphere of Venus from NIMS-Galileo. Planet. Space Sci. 41, 495–504, doi:10.1016/0032-0633(93)90032-W, 1993.

Drossart, P. et al. A dynamic upper atmosphere of Venus as revealed by VIRTIS on Venus Express. Nature 450, 641–645, doi:10.1038/nature06140, 2007a.

Drossart, P. et al. Scientific goals for the observation of Venus by VIRTIS on ESA/Venus Express mission. Planet. Space 55, 1653–1672, doi:10.1016/j.pss.2007.01.003, 2007b.

Gérard, J.-C., Saglam, A., Piccioni, G., Drossart, P., Cox, C., Erard, S., Hueso, R., Sánchez-Lavega, A. Distribution of the O_2 infrared nightglow observed with VIRTIS on board Venus Express. Geophys. Res. Lett. 35, 2207, doi:10.1029/2007GL032021, 2008.

Gérard, J.-C., Saglam, A., Piccioni, G., Drossart, P., Montmessin, F., Bertaux, J.-L. Atomic oxygen distribution in the Venus mesosphere from observations of O_2 infrared airglow by VIRTIS-Venus Express. Icarus 199, 264–272, doi:10.1016/j.icarus.2008.09.016, 2009.

Hueso, R., Sánchez-Lavega, A., Piccioni, G., Drossart, P., Gérard, J.-C., Khatuntsev, I., Zasova, L. Morphology and dynamics of Venus oxygen airglow. J. Geophys. Res. 113, E00B02, doi:10.1029/2008JE003081, 2008.

Krasnopolsky, V.A. Venus night airglow: ground-based detection of OH, observations of O_2 emissions, and photochemical model. Icarus, doi:10.1016/j.icarus.2009.10.019, in press, 2010.

Lellouch, E., Clancy, T., Crisp, D., Kliore, A., Titov, D., Bougher, S.W. Monitoring of mesospheric structure and dynamics, in: Bougher, S.W., Hunten, D.M., Philips, R.J. (Eds.), Venus II: Geology, Geophysics, Atmosphere, and Solar, Wind Environment. The Univ. of Arizona Press, Tucson, 1997.

Meriwether Jr., J.W. A review of the photochemistry of selected nightglow emissions from the mesopause. J. Geophys. Res. 94, 14,629–14,646, 1989.

Montmessin, F., Bertaux, J.L., Lefèvre, F., Vandaele, A.C., Korablev, O., Marcq, E., Fedorova, Royer, A., Mahieux, E., Belyaev, A.D., Wilquet, V. Discovery of an ozone layer on Venus by SPICAV on Venus Express. Bull. Am. Astronom. Soc. 41 (3), 2009.

Ohtsuki, S., Iwagami, N., Sagawa, H., Ueno, M., Kasabac, Y., Imamura, T., Nishihara, E. Imaging spectroscopy of the Venus 1.27-μm, O_2 airglow with ground-based telescopes. Adv. Space Res. 41, 1375–1380, 2008.

Pernice, H., Garcia, P., Willner, H., Francisco, J.S., Mills, F.P., Allen, M., Yung, Y.L. Proc. Natl. Acad. Sci. 101, 14007–14010, 2004.

Piccioni, G., Drossart, P., Zasova, L., Migliorini, A., Gérard, J.-C., Mills, F.P., Shakun, A., Garcia-Munoz, A., Ignatiev, N., Grassi, D., Cottini, V., Taylor, F.W., Erard, S. The VIRTIS-Venus Express Technical Team. First detection of hydroxyl in the atmosphere of Venus. Astronom. Astrophys. 483, L29–L33, 2008.

Piccioni, G., Zasova, A., Migliorini, A., Drossart, P., Shakun, A., Garcia-Munoz, A., Mills, F.P., Cardesin-Moinelo, A. Near-IR oxygen nightglow observed by VIRTIS in the Venus upper atmosphere. J. Geophys. Res. 114, E00B38, doi:10.1029/2008JE003133, 2009.

Svedhem, H. et al. Venus express – The first European mission to Venus. Planet. Space Sci. 55, 1636–1652, doi:10.1016/j.pss.2007.01.013, 2007.

Titov, D.V. et al. Venus express science planning. Planet. Space Sci. 54, 1279–1297, doi: 10.1016/j.pss.2006.04.017, 2006.

Zhu, X., Yee, J.-H. Wave–photochemistry coupling and its effect on water vapor, ozone and airglow variations in the atmosphere of Mars. Icarus 189, 136–150, doi:10.1016/j.icarus.2007.01.006, 2007.